

ARTICLE OPEN



Fluoropolymer-based organic memristor with multifunctionality for flexible neural network system

Min-Hwi Kim¹, Hea-Lim Park², Min-Hoi Kim³, Jaewon Jang⁴, Jin-Hyuk Bae⁴, In Man Kang⁴ and Sin-Hyung Lee⁴✉

In this study, we propose an effective strategy for achieving the flexible one organic transistor–one organic memristor (1T–1R) synapse using the multifunctional organic memristor. The dynamics of the conductive nanofilament (CF) in a hydrophobic fluoropolymer medium is explored and a hydrophobic fluoropolymer-based organic memristor is developed. The flexible 1T–1R synapse can be fabricated using the solution process because the hydrophobic fluorinated polymer layer is produced on the organic transistor without degradation of the underlying semiconductor. The developed flexible synapse exhibits multilevel conductance with high reliability and stability because of the fluoropolymer film, which acts as a medium for CF growth and an encapsulating layer for the organic transistor. Moreover, the synapse cell shows potential for high-density memory systems and practical neural networks. This effective concept for developing practical flexible neural networks would be a basic platform to realize the smart wearable electronics.

npj Flexible Electronics (2021)5:34; <https://doi.org/10.1038/s41528-021-00132-w>

INTRODUCTION

Hardware-based neural network systems have been drawing attention as potential candidates for realizing the next generation of computing systems beyond von Neumann architectures^{1–4}. In such neural network systems, synaptic devices, acting as artificial synapses, are key components for achieving parallel computation^{4–6}. Until now, many studies have been conducted on the artificial synapses with 3-terminal^{7–9} and 2-terminal structures^{10–14}. Among them, solution-processed organic memristors are promising synaptic devices for wearable neural network systems and neuromorphic electronics due to their mechanical flexibility, scalability, biocompatibility, and simple and low-cost fabrication process^{15–20}. For organic memristors, a metallic conductive nanofilament (CF) is selectively formed (or ruptured), according to the electric field in the device, which results in its resistive switching characteristics^{18,19,21}. Additionally, the multilevel conductance for mimicking biorealistic neural networks can be obtained by controlling the CF growth of the device^{22,23}. Therefore, the electrochemical metallization (ECM) phenomena for CF dynamics in organic media are essential for developing organic memristors. In the ECM-based memristors, the growth of the CF is arbitrarily achieved; thus, it is barely possible to accurately program the device conductance to a target value^{19,24–27}. Recently, for inorganic systems, a driving transistor serially connected to the memristor cell has been used for practical neural networks^{28,29}. In this system, the transistor regulates the electric potential of the memristor according to the gate voltage (V_g), which leads to delicate control of the CF thickness and a reliable conductance change. However, for the case of solution-processed organic electronics, it is difficult to integrate the driving transistor with the memristor in a single substrate, because of the solvent orthogonality, which limits multi-stacking of the organic layers^{30,31}. Additionally, the poor air stability of organic semiconductors induces the degradation of the electrical performances of organic transistors under ambient conditions^{32,33}. For realizing practical wearable

neural networks, it is important to explore an effective yet simplistic strategy for achieving the one organic transistor–one organic memristor (1T–1R) structured cell with high stability.

Amorphous fluoropolymers with low permeability for gas and moisture are promising candidates for robust encapsulation^{34–36}. Particularly, a hydrophobic fluorinated polymer, poly(2,2,3,3,4,4,4-heptafluoro-butyl methacrylate) (EGC-1700), is widely used for encapsulating organic electronics due to its orthogonal solvent (methoxy-nonafluorobutane) compatible with the organic semiconductors^{37–39}. Moreover, such a fluorinated polymer can be simply coated or patterned onto the flexible substrates by transfer printing, with the delicate control of the film thickness^{38,39}. Despite the multifunctionality of the hydrophobic fluoropolymer (EGC-1700) in practical organic electronics, the ECM effect of the CF formation on such a polymer medium has not been explored, and the hydrophobic fluoropolymer-based memristor is yet to be developed.

In this study, we demonstrate a fluoropolymer-based memristor with multifunctionality for practical flexible neuromorphic systems. The CF growth in the fluoropolymer medium and the resultant resistive switching phenomenon were explored. Based on this physical analysis, we simply produced the fluoropolymer-based memristor on a flexible substrate using the transfer printing method (see Fig. 1a). The developed memristor was operated as a reliable non-volatile memory with the multilevel states, exhibiting high durability even under repeated mechanical stress. Moreover, a highly stable 1T–1R cell for the artificial synapse was realized by coating the hydrophobic fluoropolymer onto the organic transistor. In our cell, the fluoropolymer film played the role of the insulator of the organic memristor and encapsulating layer for the transistor. During the operation of the cell, the conductance of our organic memristor was reliably and stably tuned, and the sneak current path was effectively suppressed according to the gate bias of the transistor. In the numerical analysis, the proposed artificial

¹School of Electrical and Computer Engineering, Seoul National University, 1 Gwanak-ro, Gwanak-gu, Seoul 08826, Republic of Korea. ²Department of Materials Science and Engineering, Seoul National University of Science and Technology, Seoul 01811, Republic of Korea. ³Department of Creative Convergence Engineering, Hanbat National University, Yuseong-gu, Daejeon 305-719, Republic of Korea. ⁴School of Electronics Engineering, and School of Electronic and Electrical Engineering, Kyungpook National University, 80 Daehak-ro, Buk-gu, Daegu 702-701, Republic of Korea. ✉email: sinhlee@knu.ac.kr

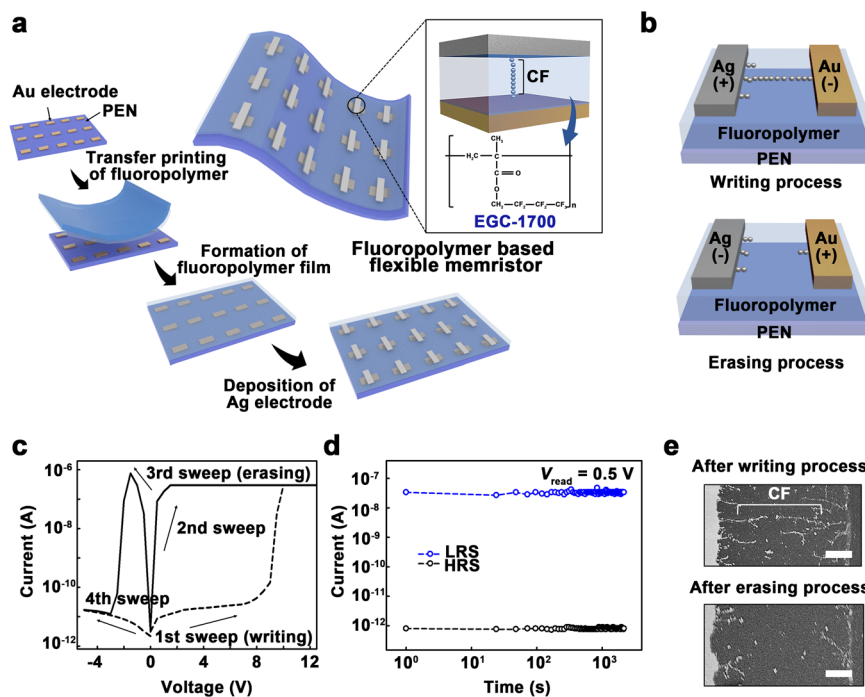


Fig. 1 Concepts and operating principles of the fluoropolymer-based flexible memristor. **a** Schematics of the fabrication process of the flexible memristors based on the fluoropolymer. Inset image shows the device configuration and the chemical structure of the fluoropolymer. **b** Schematics illustrating the fluoropolymer-based memristor with a lateral structure. The gap between the electrodes was about $4.8\ \mu\text{m}$. **c** Current–voltage curves of the lateral-type device. **d** Retention characteristics of the lateral-type device. **e** Active surfaces of the lateral-type device after the writing and erasing processes, observed by field emission scanning electron microscopy (scale bar, $1\ \mu\text{m}$).

synapse using the 1T–1R structure exhibited the potential capabilities for achieving practical neural network systems with high integration density.

RESULTS AND DISCUSSION

Dynamics of CF growth in the fluoropolymer medium

To explore the CF growth in the fluoropolymer medium, we prepared the lateral-structured organic memristor, as shown in Fig. 1b. In the organic memristor, active and inert electrodes were made of gold and silver, respectively, and EGC-1700 was utilized as the hydrophobic fluoropolymer. We first measured the current–voltage (I – V) characteristics of the device. A compliance current (CC) of $3 \times 10^{-7}\ \text{A}$ was set to prevent the breakdown of the polymer at the positive voltage sweep^{40,41}. As shown in Supplementary Fig. 1, for the first positive voltage sweep, the current level was abruptly increased at 43 V, which is similar to the electroforming phenomenon of a typical memristor^{42,43}. After the sweeping process, the device exhibited the resistive switching properties in a bipolar mode (see Fig. 1c). During the writing (or erasing) process, the device was switched from the high resistance state (HRS) to the low resistance state (LRS) (or the LRS to the HRS). Additionally, each resistance state was maintained stably for $>2000\ \text{s}$, as presented in Fig. 1d. Considering that, in the writing process, the charge transport followed the space charge-limited conduction, consisting of three different regions (the Ohmic, Child’s law, and sharp conductance increase regions), the device was governed by the ECM mechanism (see Supplementary Fig. 2)^{24,44,45}. To clearly confirm the operating principle of the fluoropolymer-based memristor, the active surface of the device was investigated in each resistance state (the LRS and HRS) using field emission scanning electron microscopy, as shown in Fig. 1e. After the writing process, the multiple metallic CFs were observed, being consistent with the I – V characteristics of the device (see Fig. 1c). In the I – V curves of the device, the erasing current was higher than the CC

value, being indicative of an overgrowth of the CF. It should be noted that the current in a memristor can exceed the CC value due to the stored charges¹⁷. In the HRS, the CFs were completely ruptured. These results mean that the resistive switching phenomena in our organic memristor are mainly attributed to the formation and rupture of the CFs. Moreover, in the energy-dispersive X-ray spectroscopy measurement, the CF was found to be composed of silver (Ag), as shown in Supplementary Fig. 3.

Development of fluoropolymer-based flexible memristor

We now discuss the performance of a vertical-type flexible memristor based on the fluoropolymer from the viewpoint of its electrical characteristics and mechanical flexibility, as shown in Fig. 2a. In fabricating the device, the fluoropolymer film was simply prepared by transfer printing, and its thickness was about 280 nm. Figure 2b shows the I – V curves of the device measured at the same CC as the value in Fig. 1c. To trigger the formation of the CF, an electroforming process was utilized (see Supplementary Fig. 4)^{42,43}. The device was operated stably as a non-volatile memory, which is consistent with the result in Fig. 1. The operating voltages for resistive switching were about 1.5 and $-1.0\ \text{V}$ for writing and erasing, respectively, and the current on/off ratio of the device was about 10^5 , which is comparable to those of the inorganic ECM memristors with high performances^{46,47}. Note that the switching voltages of the vertical-type device were smaller than those of the device with the lateral structure (see Fig. 1c) due to the narrower gap between the electrodes⁴⁸. To specifically evaluate the device memory performance, we performed the retention and cycle tests, as shown in Fig. 2c, d. At the reading voltage of 0.4 V, our memristor exhibited the constant current levels in the HRS and LRS for $5 \times 10^3\ \text{s}$ without deterioration, and the device resistance was reliably switched from the HRS to the LRS (or vice versa) during the repeated cycles, consisting of the writing and erasing processes. This implies that our reliable device can be used in memory applications of flexible electronics. Another important

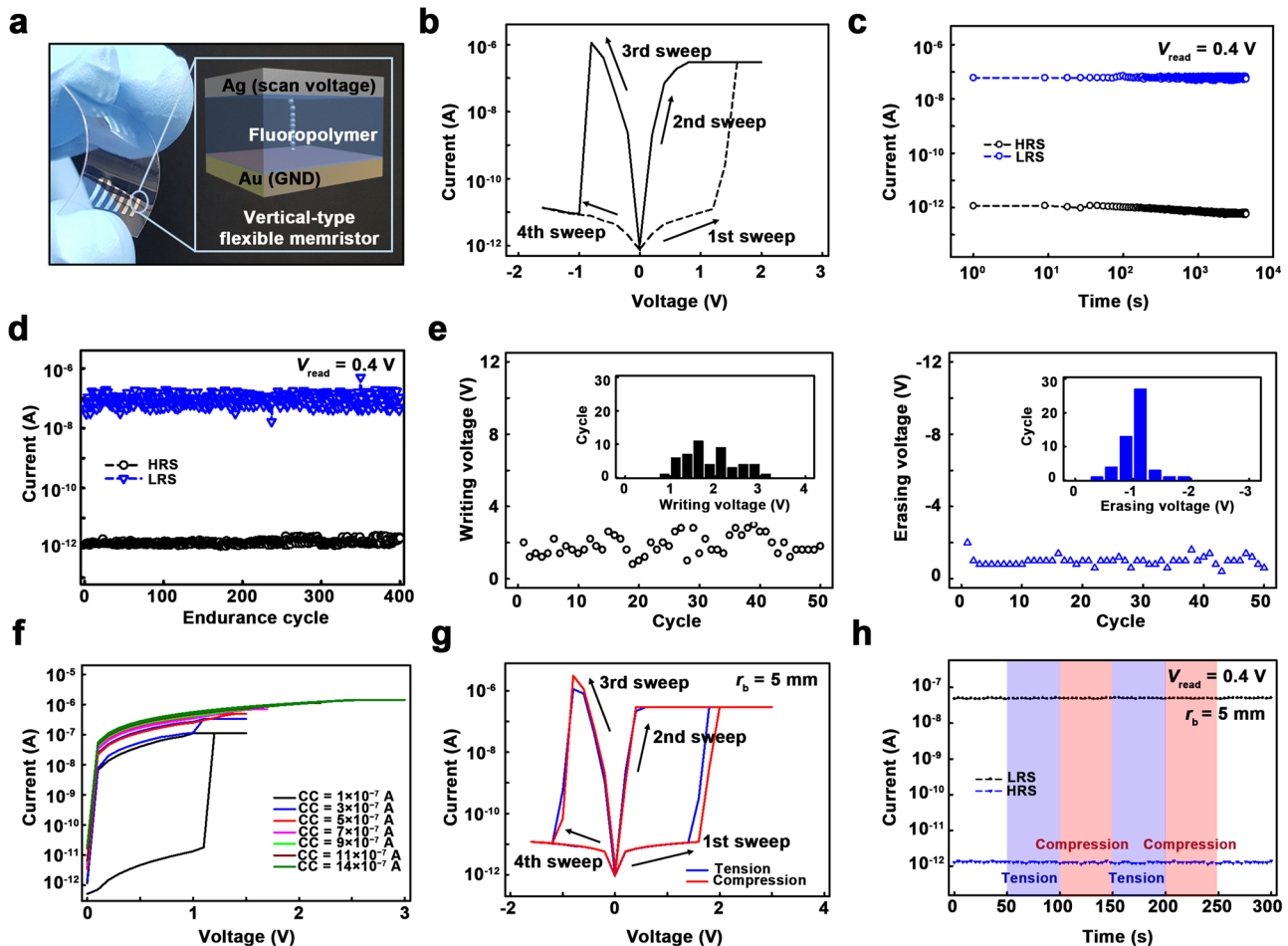


Fig. 2 Electro-mechanical characteristics of the fluoropolymer-based flexible memristor. **a** Photographic image of the vertical-type flexible memristor under bending deformation. Inset image shows a structure of the memristor. The thickness of the polymer film was about 280 nm, and the active area of the device was 0.5 mm \times 0.5 mm. **b** Current–voltage (I – V) curves of the device. **c** Retention performances of the device. **d** Electrical endurance characteristics of the device. **e** Distributions of the switching voltages of the device in the repeated cycle tests. **f** Demonstration of the multilevel conductance in the device. **g** I – V properties of the device under bending stresses with a radius of 5 mm. **h** Retention characteristics measured with the repeated bending stresses with a radius of 5 mm.

property of the memristor for practical systems is the reproducibility of the switching voltages^{49,50}. We investigated the changes in the writing and erasing voltages for 50 cycles, as shown in Fig. 2e. The temporal variations estimated by the ratio of the standard deviation to the mean were about 0.29 and 0.27 for writing and erasing voltages, respectively, which are comparable to those of the typical ECM organic memristors previously reported¹⁷. Supplementary Fig. 5 shows the switching voltage distributions for 12 different cells. Although the switching voltages of the devices were slightly different from each other by the arbitrary growth of the CF, we can effectively improve the reliability of the resistive switching by introducing the interfacial metallic sites for local electric field enhancement^{27,51,52}. Additionally, we demonstrated the multilevel conductance in the device by controlling the CF growth (see Fig. 2f). The CC values were changed in the writing process to tune the CF thickness and the resultant device conductance^{48,53}. Note that the multilevel state is an essential condition for realizing the high-density memory and neuromorphic systems^{6,23}. In this regard, we can consider that our device can act as a crucial component not only in the memory systems but also in the hardware-based neural networks. For memory applications, the pulse operation of the device is necessary for high speed and low power consumption^{54,55}. As

shown in Supplementary Fig. 6, we measured the transient response of the fluoropolymer-based memristor in a pulse mode. The device exhibited the stable resistive switching performances under voltage pulses with amplitudes of 3.5 V (for writing) and -2.0 V (for erasing), and the switching times for writing and erasing were about 70 and 60 μ s, respectively. It should be noted that the CF formation is highly dependent on the voltage parameters including the bias time and the voltage amplitude¹⁸. The operating speed of our device can be effectively improved through the amplitude of the voltage pulse.

Further, we discuss the mechanical durability of the fluoropolymer-based flexible memristor. The positive and negative bending deformations with a curvature radius of 5 mm were conducted for evaluating the device durability for compressive and tensile stresses, respectively (see Supplementary Fig. 7). As presented in Fig. 2g, under the bending stresses, our device exhibited the stable resistive switching characteristics similar to that in its flat state (see Fig. 2b). Figure 2h shows the influence of mechanical deformations on the retention performance of the device. Regardless of the repeated stresses for 200 s, the device conductance was stably maintained, which implies that our developed organic memristor possesses superior endurance for mechanical deformations^{17,18}.

Realization of flexible 1T-1R synapse cell

We then developed a flexible artificial synapse with the 1T-1R structure by simply stacking the fluoropolymer-based memristor onto an organic transistor, as shown in Fig. 3a. The memristor was connected, serially, to the source electrode of the organic transistor. For the organic transistor, we utilized a pentacene film with 50 nm thickness as the semiconducting layer. Figure 3b shows the transfer curve of the organic transistor, according to the V_g from 10 to -50 V at several drain voltage (V_d) values. The channel conductance of the transistor was effectively varied by V_g , indicating that the CC for regulating the electric potential at the organic memristor can be defined and delicately tuned by the transistor. It should be noted that the control of the external CC values is an effective way for achieving multilevel conductance in ECM memristors^{48,53}. Additionally, in the organic transistor, the leakage current was stably suppressed during the repeated voltage sweeps, as shown in Supplementary Fig. 8a.

In our synapse, the hydrophobic fluoropolymer acting as the insulator of the memristor completely, covered the organic transistor, thus the transistor was completely protected from the moisture in the air. To confirm the capability of the fluoropolymer as an encapsulation layer, we performed the gate bias stress test for the organic transistor^{56,57}. A constant V_g of -40 V was applied to the transistor for 1000 s in the stress test. As shown in Fig. 3c, we compared the transfer curves of the device measured in the initial state and after the bias stress. For both cases, the device exhibited a reliable operation without hysteresis because of the gate insulator of poly(methyl methacrylate) (PMMA)⁵⁶ in PMMA, methyl methacryl groups with low polarity have a relatively low degree of water permeability than other polymer materials. In addition, the PMMA film stably played as the electrical insulator that suppresses the leakage current (see Supplementary Fig. 8b). In our organic transistor, the mobility (about $0.15 \text{ cm}^2 \text{ V}^{-1} \text{ s}^{-1}$) was not changed regardless of the bias stress, and the threshold voltage shift was about 1.0 V, which is much lower than that of the

previously reported non-capsulated device, which had the same structure as our device⁵⁶. This implies that the fluoropolymer layer effectively prevents the exposure of the transistor to moisture. Supplementary Fig. 9 shows the I - V characteristics of our 1T-1R cell. For the writing process, V_g and the voltage for the active electrode were fixed at -20 and 0 V, respectively, and V_d was controlled. Contrarily, in the erasing process, an active electrode bias was changed at $V_g = -50$ V and $V_d = 0$ V. The cell exhibited the stable resistive-switching characteristics, and the increased current level was saturated to a target value without an external CC of the measurement system, which was an indicator of the accurately tuned conductance. As shown in Supplementary Figs. 10 and 11, the developed 1T-1R cell showed the highly improved reliability and device-to-device uniformity, compared to those of the single fluoropolymer-based memristor, due to the regulated CF growth. Moreover, the developed organic cell can be used for developing high-density memory systems with a crossbar configuration because the sneak current paths are selectively suppressed according to V_g . An integration density of the crossbar array based on our cell was theoretically calculated to be larger than about 8.7 Mbit in the floating scheme, which is superior to previous studies (see Supplementary Fig. 12)^{58,59}. In realizing vector-matrix multiplication for the neural network, the reliable multilevel conductance and its stable retention performance are very important factors of an artificial synapse^{2,4}. We measured the multilevel conductance of the synapse cell under the pulse mode. In the 1T-1R cell, the CF growth and the resultant conductance of the memristor can be precisely controlled at the writing process by the transistor. Thus, during the consecutive writing processes, we controlled the value of V_g for achieving the linear conductance change. For potentiation, the amplitude and width of the V_d pulse were -2.5 V and 100 ms, respectively, and the V_g value was decreased from -17 to -35 V. In contrast, in the depression process, the voltage pulse of -2.5 V for 100 ms was applied to the active electrode of the memristor, and the V_g was fixed at -50 V.

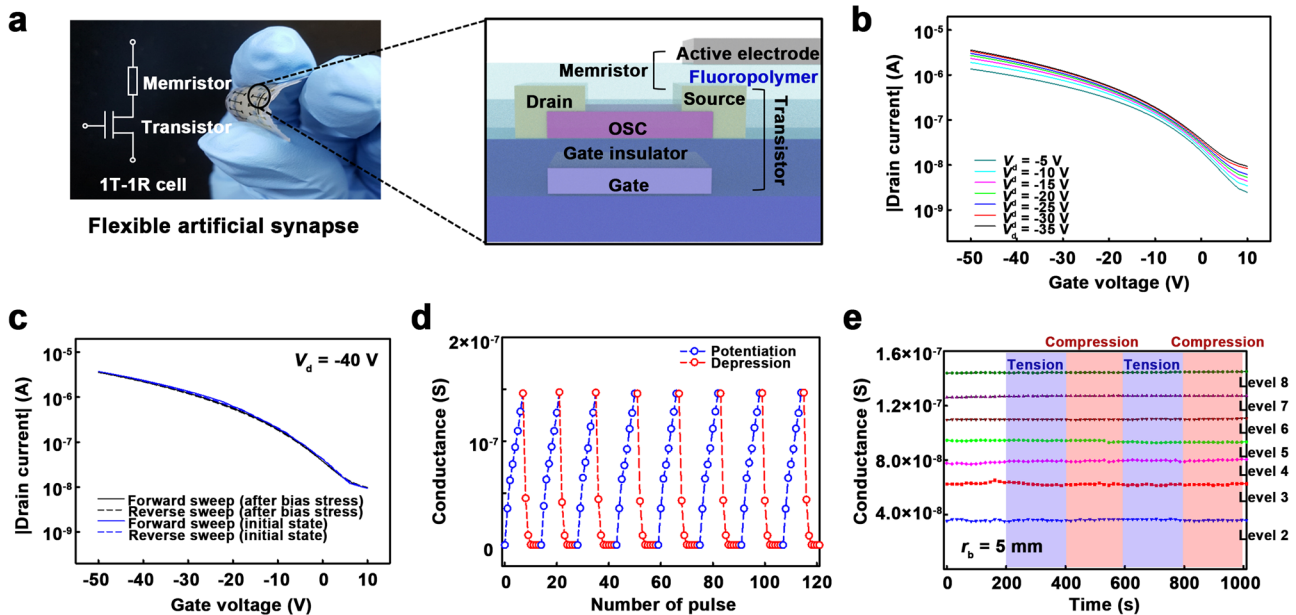


Fig. 3 Electro-mechanical characterization of the artificial synapse cells. **a** Photographic image of the flexible artificial synapse under a bending stress. Inset image shows the schematics illustrating the developed synapse cell structure. For the organic transistor, 50-nm-thick pentacene was used as the semiconducting layer. The channel width and length of the transistor were 1 mm and 150 μm , respectively. The thickness of the fluoropolymer film was 320 nm, and the active area of the memristor was 0.15 mm \times 0.5 mm. **b** Transfer characteristics of the organic transistor for the synapse cell. **c** Transfer characteristics of the organic transistor in the initial state and after the application of bias stress. For the bias stress, the gate voltage of -40 V was applied to the device for 1000 s. **d** Reliable multilevel memory properties of the artificial synapse. **e** Mechanical and electrical stabilities of the synapse in seven memory states.

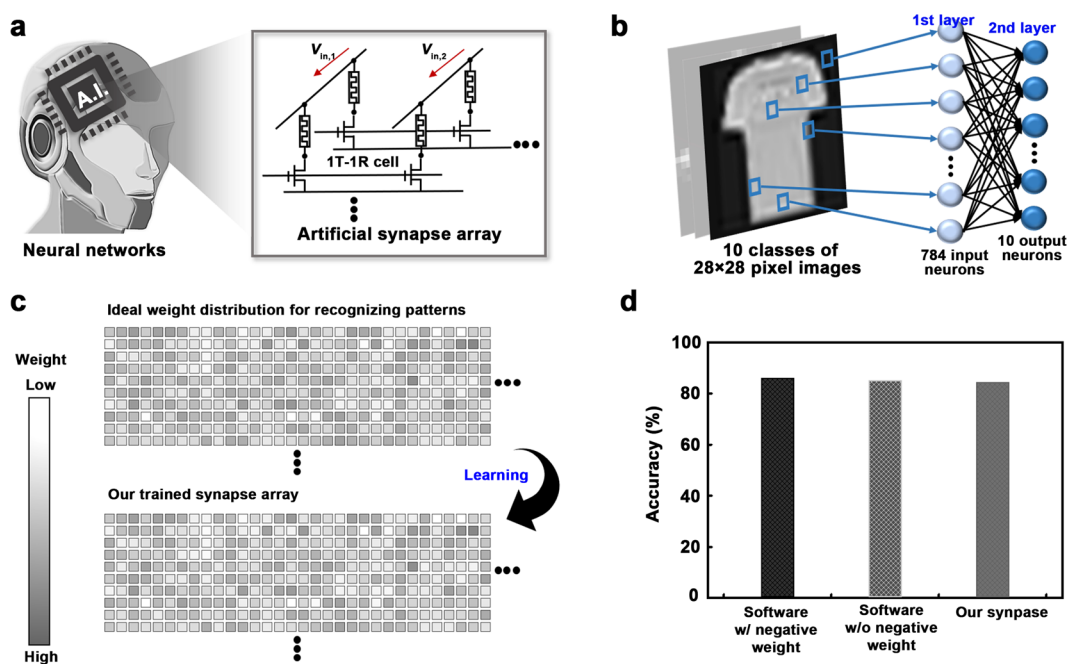


Fig. 4 Pattern recognition in neural networks based on the developed synapse array. **a** Schematics presenting the 1T–1R structured crossbar array and its applications. **b** A fully connected one-layer neural network for the recognition of labeled fashion images. The input (784 neurons for input images with 28×28 pixels) and output (10 neurons for 10 classes of images) neurons were used. **c** Distributions of ideal synaptic weights for the accurate pattern recognition (top) and the weights of the trained synapse arrays after the learning process (bottom). **d** Recognition accuracy after training 10 epochs for an ideal software and the developed synapse-based neural networks.

Note that the active electrode bias for potentiation and V_d for depression were grounded. Under the potentiation, our cell exhibited the relatively superior linearity in the conductance change, compared to the previous studies⁶⁰ (see Supplementary Fig. 13). Moreover, as shown in Fig. 3d, the conductance of the cell was reliably changed in the repeated potentiation processes. Although the conductance ratio (about 4) is restricted by the conventional organic transistor with the low on/off ratio (about 5×10^2) (see Fig. 3b), it can be effectively enhanced by utilizing the transistor device with the high on/off ratio.

Let us discuss about the electrical and mechanical stability of our 1T–1R cell. As shown in Supplementary Figs. 14 and 15, under the memory retention and bending cycle tests, the cell showed the stable eight different conductance states⁵⁸. Figure 3e presents the mechanical and electrical stabilities of the cell at seven different LRSs. We applied the successive negative and positive bending stresses to the cell for 800 s, at the memory retention test. In all states, the conductance was maintained without any degradation, which means that our 1T–1R cell is a promising component for practical flexible neural networks^{17,58,59}.

Pattern-recognition capability of developed synapse array

Hardware-based neural networks can be used in various artificial intelligence applications, such as pattern-recognition systems^{1,4}, as shown in Fig. 4a. To specifically analyze the potentials of the developed 1T–1R synapse for realizing hardware-based neural networks, the SPICE simulation for pattern recognition was carried out by using a dataset from the Fashion Modified National Institute of Standards and Technology (MNIST), as shown in Fig. 4b. The Fashion MNIST dataset is composed of 70,000 grayscale images (10,000 images for test and 60,000 images for training) for 10 categories of fashion images. It is known to be more difficult to obtain high classification accuracy in the Fashion MNIST than the commonly used original MNIST for handwritten digits^{61,62}. For the

pattern-recognition simulation, we set a simple one-layer neural network with general conditions, and the input (784 neurons for input images with 28×28 pixels) and output (10 neurons for 10 classes of fashion images) neurons were used. In all, 784×10 synapses in the connected network were trained, and only the non-negative weight was used to effectively transfer the weight value to the conductance of the hardware synapse cell. Note that the performance of the neural network based on the non-negative weight constraint was similar to that of the system with a pair of synapses for the negative weight in the software-based numerical simulation (see Supplementary Fig. 16). Each synapse consisted of our 1T–1R cell (see the inset image in Fig. 4a), and the cell parameters, estimated in Fig. 3d, were used. Details for the simulation conditions are as follows. For the software training level, we adopted softmax activation function for the output value⁶³. During the training process, we used the adaptive momentum estimation optimizer⁶⁴ and the sparse categorical crossentropy loss function⁶⁵. In the SPICE simulations for evaluating the hardware-based neural networks, we converted the weight value obtained in the training process into the conductance of the cell on the synapse array and in some cases quantize it to a specific level. Figure 4c shows the weight distributions of the synapse array after the converting process. Each synaptic weight of the cell was found to be close to the target value, which is ideal for recognizing the fashion images of MNIST, indicating that our 1T–1R synapse with the reliable multilevel conductance is promising for offline learning systems⁶¹. For inference that is quite similar to the read operation of the memory array, the input voltage between 0 and 1 V was set, and the output current of each bit line was checked. In our trained system, the accuracy for recognizing the fashion images was about 85% (see Fig. 4d), similar to that of the ideal software-based neural networks, consistent with the result shown in Fig. 4c. Note that, the learning accuracy

increases with epochs at the initial training stage, but it tends to saturate after 10 epochs due to the convergent characteristics of the neural networks⁶⁶, as shown in Supplementary Fig. 17. In addition, in the simulations for the handwritten digits based on the original MNIST, our neural network system exhibited the classification accuracy of about 93% (see Supplementary Fig. 18), which is close to that of the ideal software system.

In conclusion, we demonstrated the flexible artificial synapse with the 1T–1R configuration for practical hardware-based neural network systems. We developed a hydrophobic fluoropolymer-based memristor that can be simply printed onto the organic transistor without damage to the underlying semiconducting layer. We found that the metallic CF was effectively grown at the hydrophobic fluoropolymer medium based on the amplitude of an electric potential. In our proposed artificial synapse, composed of the fluoropolymer-based memristor integrated with the organic transistor, the hydrophobic fluorinated film, acting as an insulator of the memristor, prevented the moisture diffusion to the transistor, and thus the stability of the device was highly enhanced. Our synapse showed the linearly and accurately tunable multilevel conductance, which is essential for realizing practical neural networks. Moreover, under the repeated bending stresses, the device was operated stably with high mechanical durability. In developing the flexible memory systems, the proposed synapse array with the 1T–1R structure showed an integration density >8.7 Mbit. Additionally, our synapse showed the capability for realizing hardware-based neural networks. The neural networks based on our synapse achieved about 85% accuracy for the complex image recognition, which is similar to the ideal software system. This effective strategy for developing practical and flexible neural networks would provide a basic platform for achieving the next generation of wearable electronics linked to artificial intelligence.

METHODS

Characterization

The geometrical profiles of all devices were investigated utilizing an atomic force microscopy (XE-100, PSIA). The electrical performances of the devices were measured utilizing a semiconductor parameter analyzer (4200-SCS, Keithley) and an ultrafast *I*–*V* module (4225-PMU, Keithley). In testing the electrical characteristics of the organic memristors, the scanning voltage was applied to the active electrode (Ag), and the inert electrode (Au) was grounded. The CF growth in the polymer medium was analyzed through a field-emission scanning electron microscope (JSM-7401F, JEOL) and an energy-dispersive X-ray spectrometer (AZtec Energy, Oxford).

Fabrication of hydrophobic fluoropolymer-based memristor

To fabricate the fluoropolymer-based memristor, first, a polyethylene naphthalate (PEN) substrate was cleaned under ultrasonication in acetone, isopropyl alcohol, and deionized water in sequence for 30 min. As the inert electrode, a gold layer with thickness of 50 nm was thermally evaporated at 0.5 \AA s^{-1} under 10^{-6} Torr. To form the fluoropolymer layer, predefined fluoropolymer film (NovocTM EGC-1700, 3 M) was transfer-printed on the cleaned substrate using the gold electrode through an elastomeric stamp made of poly(dimethylsiloxane). The thickness of the fluorinated polymer film was 280 nm. For the active electrode, a 50-nm-thick silver layer was deposited using thermal evaporation at 0.8 \AA s^{-1} under 10^{-6} Torr. The active area of the device was $0.5 \text{ mm} \times 0.5 \text{ mm}$.

Fabrication of flexible 1T–1R synapse

In fabricating the flexible artificial synapse, an indium–tin–oxide (ITO) patterned PEN substrate was cleaned under ultrasonication in acetone, isopropyl alcohol, and deionized water in sequence for 30 min. Note that the ITO patterns on the substrate played as the gate electrode of the organic transistor. As the gate insulator, PMMA (Sigma-Aldrich) dissolved in anisole at a concentration of 9 wt% was deposited on the substrate by

spin-coating at 3000 rpm for 60 s. To prepare the organic semiconductor layer of the organic transistor, 50-nm-thick pentacene (Sigma-Aldrich) film was thermally evaporated on the gate insulator at the rate of 0.5 \AA s^{-1} under pressure of 7×10^{-6} Torr. For the source and drain electrodes, gold patterns with 50-nm thickness were thermally deposited at the rate of 1.0 \AA s^{-1} under 7×10^{-6} Torr. The channel width and length of the transistor were 1 mm and 150 μm , respectively. We produced the fluoropolymer film, which acted as the encapsulating layer and insulator for the organic memristor, on the transistor by dip-coating EGC-1700 in a fluorinated solvent (HFE-7100DL, 3M) at the speed of 200 mm min^{-1} . The thickness of the fluoropolymer film was 320 nm, and the source electrode of the transistor served as the inert electrode of the organic memristor. As the active electrode of the memristor, a silver layer with 50-nm thickness was thermally deposited at 0.8 \AA s^{-1} under 10^{-6} Torr. The active area of the memristor was $0.15 \text{ mm} \times 0.5 \text{ mm}$.

DATA AVAILABILITY

The data that support the findings of this study are available from the corresponding author upon reasonable request.

CODE AVAILABILITY

Code is available from the corresponding author upon reasonable request.

Received: 18 July 2021; Accepted: 29 November 2021;

Published online: 17 December 2021

REFERENCES

- Kim, S., Lim, M., Kim, Y., Kim, H.-D. & Choi, S.-J. Impact of synaptic device variations on pattern recognition accuracy in a hardware neural network. *Sci. Rep.* **8**, 2638 (2018).
- Joshi, V. et al. Accurate deep neural network inference using computational phase-change memory. *Nat. Commun.* **11**, 2473 (2020).
- Xiang, Y. et al. Efficient and robust spike-driven deep convolutional neural networks based on NOR flash computing array. *IEEE Trans. Electron Devices* **67**, 2329–2335 (2020).
- Seo, S. et al. Artificial van der Waals hybrid synapse and its application to acoustic pattern recognition. *Nat. Commun.* **11**, 3936 (2020).
- Zhu, L. Q., Wan, C. J., Guo, L. Q., Shi, Y. & Wan, Q. Artificial synapse network on inorganic proton conductor for neuromorphic systems. *Nat. Commun.* **5**, 3158 (2014).
- Berco, D. et al. Nanoscale conductive filament with alternating rectification as an artificial synapse building block. *ACS Nano* **12**, 5946–5955 (2018).
- Zhou, Y., Li, J., Yang, Y., Chen, Q. & Zhang, J. Artificial synapse emulated through fully aqueous solution-processed low-voltage In_2O_3 thin-film transistor with Gd_2O_3 solid electrolyte. *ACS Appl. Mater. Interfaces* **12**, 980–988 (2020).
- Park, H.-L. et al. Retina-inspired carbon nitride-based photonic synapses for selective detection of UV light. *Adv. Mater.* **32**, 1906899 (2020).
- Liu, D., Shi, Q., Dai, S. & Huang, J. The design of 3D-interface architecture in an ultralow-power, electrospun single-fiber synaptic transistor for neuromorphic computing. *Small* **16**, 1907472 (2020).
- Li, B. et al. Mediating short-term plasticity in an artificial memristive synapse by the orientation of silica mesopores. *Adv. Mater.* **30**, 1706395 (2018).
- Lee, T.-H. et al. Synaptic plasticity and metaplasticity of biological synapse realized in a KNbO_3 memristor for application to artificial synapse. *ACS Appl. Mater. Interfaces* **10**, 25673–25682 (2018).
- Kumar, M., Abbas, S., Lee, J.-H. & Kim, J. Controllable digital resistive switching for artificial synapses and pavlovian learning algorithm. *Nanoscale* **11**, 15596–15604 (2019).
- Feng, X. et al. A fully printed flexible MoS_2 memristive artificial synapse with femtojoule switching energy. *Adv. Electron. Mater.* **5**, 1900740 (2019).
- Sun, Y., He, N., Wen, D. & Sun, F. The nonvolatile resistive switching memristor with Co-Ni layered double hydroxide hybrid nanosheets and its application as a artificial synapse. *Appl. Surf. Sci.* **564**, 150452 (2021).
- van de Burgt, Y. et al. A non-volatile organic electrochemical device as a low-voltage artificial synapse for neuromorphic computing. *Nat. Mater.* **16**, 414–418 (2017).
- Wu, C., Kim, T. W., Choi, H. Y., Strukov, D. B. & Yang, J. J. Flexible three-dimensional artificial synapse networks with correlated learning and trainable memory capability. *Nat. Commun.* **8**, 752 (2017).
- Park, H.-L., Kim, M.-H. & Lee, S.-H. Introduction of interfacial load polymeric layer to organic flexible memristor for regulating conductive filament growth. *Adv. Electron. Mater.* **6**, 2000582 (2020).

18. Park, H.-L., Kim, M.-H., Kim, M.-H. & Lee, S.-H. Reliable organic memristors for neuromorphic computing by predefining a localized ion-migration path in crosslinkable polymer. *Nanoscale* **12**, 22502–22510 (2020).
19. Lee, S.-H. et al. Realization of biomimetic synaptic functions in a one-cell organic resistive switching device using the diffusive parameter of conductive filaments. *ACS Appl. Mater. Interfaces* **12**, 51719–51728 (2020).
20. Lee, Y., Park, H.-L., Kim, Y. & Lee, T.-W. Organic electronic synapses with low energy consumption. *Joule* **5**, 794–810 (2021).
21. Park, H.-L., Kim, M.-H. & Lee, S.-H. Control of conductive filament growth in flexible organic memristor by polymer alignment. *Org. Electron.* **87**, 105927 (2020).
22. Zeng, F., Li, S., Yang, J., Pan, F. & Guo, D. Learning processes modulated by the interface effects in a Ti/conducting polymer/Ti resistive switching cell. *RSC Adv.* **4**, 14822–14828 (2014).
23. Jang, B. C. et al. Polymer analog memristive synapse with atomic-scale conductive filament for flexible neuromorphic computing system. *Nano Lett.* **19**, 839–849 (2019).
24. Sun, Y. et al. Guiding the growth of a conductive filament by nanoindentation to improve resistive switching. *ACS Appl. Mater. Interfaces* **9**, 34064–34070 (2017).
25. Zhao, X. et al. Confining cation injection to enhance CBRAM performance by nanopore graphene layer. *Small* **13**, 1603948 (2017).
26. Choi, S. et al. SiGe epitaxial memory for neuromorphic computing with reproducible high performance based on engineered dislocations. *Nat. Mater.* **17**, 335–340 (2018).
27. Lee, S.-H., Park, H.-L., Kim, M.-H., Kang, S. & Lee, S.-D. Interfacial triggering of conductive filament growth in organic flexible memristor for high reliability and uniformity. *ACS Appl. Mater. Interfaces* **11**, 30108–30115 (2019).
28. Yao, P. et al. Fully hardware-implemented memristor convolutional neural network. *Nature* **577**, 641–646 (2020).
29. Zhao, X. et al. Photoassisted electroforming method for reliable low-power organic–inorganic perovskite memristors. *Adv. Funct. Mater.* **30**, 1910151 (2020).
30. Gaikwad, A. M. et al. Identifying orthogonal solvents for solution processed organic transistors. *Org. Electron.* **30**, 18–29 (2016).
31. Lee, S.-H., Park, H.-L., Kang, S., Kim, M.-H. & Lee, S.-D. Organic thin-film transistors with liquid crystalline polymer insulator integrated for solution-processed organic light-emitting devices. *Semicond. Sci. Technol.* **34**, 105012 (2019).
32. Feng, L. et al. Unencapsulated air-stable organic field effect transistor by all solution processes for low power vapor sensing. *Sci. Rep.* **6**, 20671 (2016).
33. Huang, K.-M. et al. 2-V operated flexible vertical organic transistor with good air stability and bias stress reliability. *Org. Electron.* **50**, 325–330 (2017).
34. Zan, H.-W. & Hsu, T.-Y. Stable encapsulated organic TFT with a spin-coated poly(4-vinylphenol-co-methyl methacrylate) dielectric. *IEEE Electron Device Lett.* **32**, 1131–1133 (2011).
35. Jeon, J.-Y. & Ha, T.-J. Waterproof electronic-bandage with tunable sensitivity for wearable strain sensors. *ACS Appl. Mater. Interfaces* **8**, 2866–2871 (2016).
36. Ji, X. et al. Smart surgical catheter for C-reactive protein sensing based on an imperceptible organic transistor. *Adv. Sci.* **5**, 1701053 (2018).
37. Jackson, N., Anand, S., Okandan, M. & Muthuswamy, J. Nonhermetic encapsulation materials for MEMS-based movable microelectrodes for long-term implantation in the brain. *J. Microelectromech. Syst.* **18**, 1234–1245 (2009).
38. Choi, W., Kim, M.-H., Na, Y.-J. & Lee, S.-D. Complementary transfer-assisted patterning of high-resolution heterogeneous elements on plastic substrates for flexible electronics. *Org. Electron.* **11**, 2026–2031 (2010).
39. Keum, C.-M., Bae, J.-H., Kim, M.-H., Choi, W. & Lee, S.-D. Solution-processed low leakage organic field-effect transistors with self-pattern registration based on patterned dielectric barrier. *Org. Electron.* **13**, 778–783 (2012).
40. Siddiqui, G. U., Rehman, M. M. & Choi, K. H. Enhanced resistive switching in all-printed, hybrid and flexible memory device based on perovskite ZnSnO₃ via PVOH polymer. *Polymer* **100**, 102–110 (2016).
41. Sun, Y. & Wen, D. Conductance quantization in nonvolatile resistive switching memory based on the polymer composite of zinc oxide nanoparticles. *J. Phys. Chem. C* **122**, 10582–10591 (2018).
42. Qian, K., Nguyen, V. C., Chen, T. & Lee, P. S. Amorphous-Si-based resistive switching memories with highly reduced electroforming voltage and enlarged memory window. *Adv. Electron. Mater.* **2**, 1500370 (2016).
43. Zhu, Y. B., Zheng, K., Wu, X. & Ang, L. K. Enhanced stability of filament-type resistive switching by interface engineering. *Sci. Rep.* **7**, 43664 (2017).
44. Gao, L., Lee, S. B., Hoskins, B., Yoo, H. K. & Kang, B. S. Dynamic switching mechanism of conduction/set process in Cu/a-Si/Si memristive device. *Appl. Phys. Lett.* **103**, 043503 (2013).
45. Wu, M.-C., Ting, Y.-H., Chen, J.-Y. & Wu, W.-W. Low power consumption nanoflamentary ECM and VCM cells in a single sidewall of high-density VRRAM arrays. *Adv. Sci.* **6**, 1902363 (2019).
46. Kim, S. et al. Neuronal dynamics in HfO₂/AlO_y-based homeothermic synaptic memristors with low-power and homogeneous resistive switching. *Nanoscale* **11**, 237–245 (2019).
47. Lee, J. et al. Synaptic characteristics of amorphous boron nitride-based memristors on a highly doped silicon substrate for neuromorphic engineering. *ACS Appl. Mater. Interfaces* **12**, 33908–33916 (2020).
48. Lee, S.-H. et al. Organic flexible memristor with reduced operating voltage and high stability by interfacial control of conductive filament growth. *Phys. Status Solidi RRL* **13**, 1900044 (2019).
49. Jung, Y. C. et al. Improved resistive switching characteristics of a Pt/HfO₂/Pt resistor by controlling anode interface with forming and switching polarity. *Appl. Surf. Sci.* **435**, 117–121 (2018).
50. Ling, H. et al. Controllable organic resistive switching achieved by one-step integration of cone-shaped contact. *Adv. Mater.* **29**, 1701333 (2017).
51. Liu, Q. et al. Controllable growth of nanoscale conductive filaments in solid-electrolyte-based ReRAM by using a metal nanocrystal covered bottom electrode. *ACS Nano* **4**, 6162–6168 (2010).
52. Yoon, J. H. et al. Highly improved uniformity in the resistive switching parameters of TiO₂ thin films by inserting Ru nanodots. *Adv. Mater.* **25**, 1987–1992 (2013).
53. Chen, C., Yang, Y. C., Zeng, F. & Pan, F. Bipolar resistive switching in Cu/AlN/Pt nonvolatile memory device. *Appl. Phys. Lett.* **97**, 083502 (2010).
54. Wang, Z. et al. Memristors with diffusive dynamics as synaptic emulators for neuromorphic computing. *Nat. Mater.* **16**, 101–108 (2017).
55. Najem, J. S. et al. Memristive ion channel-doped biomembranes as synaptic mimics. *ACS Nano* **12**, 4702–4711 (2018).
56. Fakher, S. J., Hassan, A. K. & Mabrook, M. F. Bias stress effect on high mobility-hysteresis free pentacene-based organic thin film transistors. *Synth. Met.* **191**, 53–58 (2014).
57. Xiang, L., Wang, W. & Gao, F. Improving mobility and stability of organic field-effect transistors by employing a tetratetracontane modifying PMMA dielectric. *IEEE Trans. Electron Devices* **63**, 4440–4444 (2016).
58. Kim, S. et al. Flexible crossbar-structured resistive memory arrays on plastic substrates via inorganic-based laser lift-off. *Adv. Mater.* **26**, 7480–7487 (2014).
59. Park, H.-L., Kim, M.-H., Kim, H. & Lee, S.-H. Self-selective organic memristor by engineered conductive nanofilament diffusion for realization of practical neuromorphic system. *Adv. Electron. Mater.* **7**, 2100299 (2021).
60. Khan, S. A. & Kim, S. Comparison of diverse resistive switching characteristics and demonstration of transitions among them in Al-incorporated HfO₂-based resistive switching memory for neuromorphic applications. *RSC Adv.* **10**, 31342–31347 (2020).
61. Kim, S. et al. Ferroelectric polymer-based artificial synapse for neuromorphic computing. *Nanoscale Horiz.* **6**, 139–147 (2021).
62. Nallagatla, V. R. et al. Complementary resistive switching and synaptic-like memory behavior in an epitaxial SrFeO_{2.5} thin film through oriented oxygen-vacancy channels. *ACS Appl. Mater. Interfaces* **12**, 41740–41748 (2020).
63. Cardarilli, G. C. et al. A pseudo-softmax function for hardware-based high speed image classification. *Sci. Rep.* **11**, 15307 (2021).
64. Lee, D. & Kim, H.-J. Restoration of full data from sparse data in low-dose chest digital tomosynthesis using deep convolutional neural networks. *J. Digit. Imaging* **32**, 489–498 (2019).
65. Zhao, B. et al. A CNN-based FBG demodulation method adopting the GAF-assisted ascending dimension of complicated signal. *Opt. Commun.* **499**, 127296 (2021).
66. Shimobaba, T. et al. Convolutional neural network-based data page classification for holographic memory. *Appl. Opt.* **56**, 7327–7330 (2017).

ACKNOWLEDGEMENTS

This work was supported by the National Research Foundation of Korea (NRF) under grant funded by the Korea Government (MSIT) (2020R1F1A1075436). This research was supported by National R&D Program through the National Research Foundation of Korea (NRF) funded by Ministry of Science and ICT (2021M3F3A2A03017764). This research was also supported by the BK21 FOUR project funded by the Ministry of Education, Korea (4199990113966).

AUTHOR CONTRIBUTIONS

M.-H.K. (Min-Hwi Kim) and S.-H.L. initiated and designed the experiments, analyzed the data, and wrote the draft of the manuscript. S.-H.L. and H.-L.P. fabricated and characterized the devices. M.-H.K. (Min-Hoi Kim) and S.-H.L. measured the electrical characteristics of the devices. J.J., J.-H.B., and I.M.K. assisted in device electrical characterizations and data analysis. S.-H.L. provided overall supervision of the work. All authors have read and approved the final manuscript.

COMPETING INTERESTS

The authors declare no competing interests.

ADDITIONAL INFORMATION

Supplementary information The online version contains supplementary material available at <https://doi.org/10.1038/s41528-021-00132-w>.

Correspondence and requests for materials should be addressed to Sin-Hyung Lee.

Reprints and permission information is available at <http://www.nature.com/reprints>

Publisher's note Springer Nature remains neutral with regard to jurisdictional claims in published maps and institutional affiliations.



Open Access This article is licensed under a Creative Commons Attribution 4.0 International License, which permits use, sharing, adaptation, distribution and reproduction in any medium or format, as long as you give appropriate credit to the original author(s) and the source, provide a link to the Creative Commons license, and indicate if changes were made. The images or other third party material in this article are included in the article's Creative Commons license, unless indicated otherwise in a credit line to the material. If material is not included in the article's Creative Commons license and your intended use is not permitted by statutory regulation or exceeds the permitted use, you will need to obtain permission directly from the copyright holder. To view a copy of this license, visit <http://creativecommons.org/licenses/by/4.0/>.

© The Author(s) 2021